SUPPORTING INFORMATION

Physical Methods:

Elemental analyses of the compounds isolated in these studies were accomplished in the University of Bar Ilan. EI mass spectra were recorded on a Q-Tof micro (UK)-micromass-waters spectrometer. 1H-spectra were recorded on a Bruker DPX300. UV/Vis spectra were recorded on a Varian Cary 5000 UV/Vis/NIR spectrophotometer. The measurements were carried out using a quartz cuvette with optical pathlength of 0.1 cm.

Cyclic voltammetry measurements were carried out using a Bio Logic SAS Sp-150 potentiostat. For all electrochemical experiments, the CH_2Cl_2 was freshly distilled under dinitrogen from calcium hydride. The cyclic voltammogram of each compound (1 mM) in CH_2Cl_2 containing $[NBu_4][PF_6]$ (0.15 M) as the background electrolyte was recorded under dinitrogen at room temperature using a Pt working electrode; a Pt wire secondary electrode, and an Ag/AgCl reference electrode. The cyclic voltammogram of each compound was referenced to the Fc^+/Fc couple that was used as an internal standard. When necessary, for compound $\mathbf{2}^-$, to avoid overlapping redox couples, the $[Fe(Cp^*)_2]^+/[Fe(Cp^*)_2]$ couple was used as the internal reference and the potentials of the redox process(es) observed were referenced to that of the Fc+/Fc couple by an independent calibration ($\Delta E_{1/2}$ (Fc^+/Fc *vs.* 60 $[Fe(Cp^*)_2]$+/$[Fe(Cp^*)_2]$, = 0.526 V). Controlled potential electrolysis measurements were performed using an Bio Logic SAS Sp-150 potentiostat. A three electrodes configuration was used in the cell, comprising a Pt gauze working electrode, a Pt wire secondary electrode contained in a fritted PTFE sleeve, and 65 a saturated Ag/AgCl. The potential at the working electrode was controlled by a Bio Logic SAS Sp-150 potentiostat.

The EPR measurements were performed with an X- band Elexsys E500 EPR spectrometer (Bruker, Karlsruhe, Germany) having Integrated frequency counter. The sample was inserted into a short 2 mm ID quarts tube and placed into a long 3 mm ID quarts tube at the ER 4122SHQ rectangular cavity of the EPR. Spectral recording parameters: Microwave power 2 mW; Modulation amplitude 10 G; Field sweep 5000 G ; # of scans 9. and for $[2\ (Py)_2]^-$ (insight of 4 b): Microwave power 2 mW; Modulation amplitude 2 G; Field sweep 800 G ; 3 of scans 16.

Experimental section:

Synthesis of $[NBu_4]_2[Ni^2LH_2]$ (2^{2-}). To a solution of $^2LH_4$ (0.1 g, 0.19 mmol) in dry methanol (6 mL), 0.38 mL of a solution of $[NBu_4](OH)$ (1 M in CH_3OH; 0.38 mmol) was added dropwise under N_2 at room temperature. Then a solution of $[Ni(OAc)_2]\bullet(H_2O)_4$ (47 mg, 0.19 mmol) in 10 mL of dry MeOH, was added to the reaction mixture, causing the colour of the solution to turn to light orange. The reaction mixture was kept at 90°C, in a pressure tube (length 50 cm, diameter 5 cm) for 24 hrs and was evaporated under vacuum yielding orange oily material 2^{2-} in 87% yield (175 mg). ^{1}H NMR (300 MHz, CD_3CN, 298 K): δ/ppm, 7.63 (d, ^4J = 3 Hz, 2H, Ar–H), 6.92 (d, ^4J = 3 Hz, 2H, Ar–H), 2.78 (s, 4H, CH_2), 3.10 (m, 16H, CH_2–$[NBu_4]$), 1.58 (m, 16H, CH_2–$[NBu_4]$), 1.41-1.25 (m, 18H, 18H, 16H, ^{t}Bu, ^{t}Bu, CH_2–$[NBu_4]$), 0.94 (t, 7.35 Hz, 24H CH_3–$[NBu_4]$). ^{13}C NMR (75 MHz, CD_3CN, 298 K): δ/ppm 160.10 (C(O)NH), 138.26 (Ar–C_{para}), 129.19 (Ar–C_{meta}), 122.39 (Ar–C_{ortho}), 59.29 (CH_2–$[NBu_4]$), 40.39 (CH_2), 35.82 (C–, ^{t}Bu), 31.88 (CH_3, ^{t}Bu), 24.40 (CH_2, $[NBu_4]$), 20.39 (CH_2, $[NBu_4]$), 13.81 (CH_3, $[NBu_4]$). MS ESI(−): m/z 289 (2^{2-},100%).UV-vis (CH_2Cl_2): λ_{max}/nm (ε/M^{-1} cm^{-1}): 319 (6094), 343(sh) (5596), 476 (247), 579(sh) (54). Elemental analysis: Calcd for $C_{64}H_{116}N_4O_4Ni\cdot CH_3OH$: C 71.29, H 10.96, N 5.11; Found: C 71.73, H 10.61, N 4.73.

DFT calculations

All theoretical calculations were performed with the ORCA program package.[1] Full geometry optimizations were carried out for all complexes using the GGA functional BP86[2-4] in combination with the TZV/P[5] basis set for all atoms and by taking advantage of the resolution of the identity (RI) approximation in the Split-RI-J variant[6] with the appropriate Coulomb fitting sets.[7] To properly model the interaction via H bonding in the complexes, the TZV/P++ basis set (the same basis set augmented with diffuse functions on all atoms) was employed for the relevant H, N and O atoms. Increased integration grids (Grid4 in ORCA convention) and tight SCF convergence criteria were used. Solvent effects were accounted for according to the experimental conditions. For that purpose, we used the CH_2Cl_2 (e= 9.08) solvent within the framework of the conductor like screening (COSMO) dielectric continuum approach.[8] The relative energies were obtained from single-point calculations using the B3LYP[9,10] functional together with the TZV/P[5] basis set. They were computed from the gas-phase optimized structures as a sum of electronic energy, thermal corrections to free energy, and free energy of solvation. g-tensors were obtained from relativistic single-point calculations using the B3LYP functional[9,10] Scalar relativistic effects were included with ZORA paired with the SARC def2-TZVP(-f) basis sets[11,12] and the decontracted def2-TZVP/J Coulomb fitting basis sets for all atoms. Increased integration grids (Grid4 and GridX4 in ORCA convention) and tight SCF convergence criteria were used in the calculation. The integration grids were increased to an integration accuracy of 11 (ORCA convention) for the metal center. Picture change effects were applied for the calculation of the hyperfine tensors. Optical properties were also obtained from single-point calculations using the hybrid functional B3LYP[9,10] and the TZV/P[5] basis set. Electronic transition energies and dipole moments for all models were calculated using time-dependent DFT (TD-DFT)[13-15] within the Tamm-Dancoff approximation.[16,17] To increase computational efficiency, the RI approximation[18] was used in calculating the Coulomb term and at least 30 excited states were calculated in each case.

References

1. Neese, F. Wiley Interdiscip. Rev. Comput. Mol. Sci. 2012, 2, 73.

2 Perdew, J. P. Phys. Rev. B 1986, 33, 8822.

3. Perdew, J. P. Phys. Rev. B 1986, 34, 7406.

4. Becke, A. D. Phys. Rev. A 1988, 38, 3098.

5. Schäfer, A.; Huber, C.; Ahlrichs, R. J. Chem. Phys. 1994, 100, 5829.

6. Neese, F. J. Comput. Chem. 2003, 24, 1740.

7. Weigend, F. PhysChemChemPhys 2006, 8, 1057.

8. Klamt, A.; Schürmann, G. J. Chem. Soc., Perkin Trans. 2 1993, 799.

9. Becke, A. D. J. Chem. Phys. 1993, 98, 1372.

10. Lee, C. T.; Yang, W. T.; Parr, R. G. Phys. Rev. B 1988, 37, 785.

11. Pantazis, D. A.; Chen, X. Y.; Landis, C. R.; Neese, F. J. Chem. Theory Comput. 2008, 908.

12. Pantazis, D. A.; Neese, F. J. Chem. Theory Comput. 2009, 5, 2229.

13. Casida, M. E., In *Recent Advances in Density Functional Methods*, Chong, D.P. Ed. World Scientific: Singapore, **1995**.

14. Stratmann, R. E.; Scuseria, G. E.; Frisch, M. J., *J. Chem. Phys.* **1998,** *109*, 8218-8224.

15. Bauernschmitt, R.; Ahlrichs, R., *Chem. Phys. Lett.* **1996**, 454-464.

16. Hirata, S.; Head-Gordon, M., *Chem. Phys. Lett.* **1999,** *314*, 291-299.

17. Hirata, S.; Head-Gordon, M., *Chem. Phys. Lett.* **1999,** *302*, 375-382.

18. Neese, F.; Olbrich, G., *Chem. Phys. Lett.* **2002**, 170-178.

Redox potentials: DFT methodology

The thermodynamics of redox reactions is quantified by redox potentials, E, that can be measured electrochemically and are related to the Gibbs free energy change (ΔG) with E = -ΔG/nF where n is the number of electrons transferred in the cell and F is the Faraday constant. Theoretical predictions of redox potentials are based on the above equation and require evaluation of ΔG for the oxidation or reduction process in question, e.g. Red(aq) ? Ox(aq) for the oxidation reaction. A common strategy for calculating the free energy change for redox reactions is based on a thermodynamic cycle linking the process in the gas phase with that in solvent as shown in the Figure below. The free energy change for the redox reaction, ΔG_{sol}, in solvent is computed from the free energy change of the gas-phase oxidation (or ionization) process (ΔG_g) and solvation free energies of the reduced/oxidized species ($\Delta G_{sol,rd}$ and $\Delta G_{sol,ox}$):

$\Delta G_{sol} = \Delta G_g + \Delta G_{sol,ox} - \Delta G_{sol,rd}$. The Gibbs free energy change of the gas-phase ΔG_g is computed from the gas-phase optimized structures as a sum of electronic energy, zero-point energy and thermal corrections. The connection between the gas and aqueous phases is made through the calculation of the solvation Gibbs free energy of the specific species. These terms were evaluted from the Gibbs free energy change of the system in vacuum and in soution using within the conductor like screening (COSMO) dielectric continuum approach. All redox potentials are reported here as relative potentials referenced to standard hydrogen electrode (SHE).

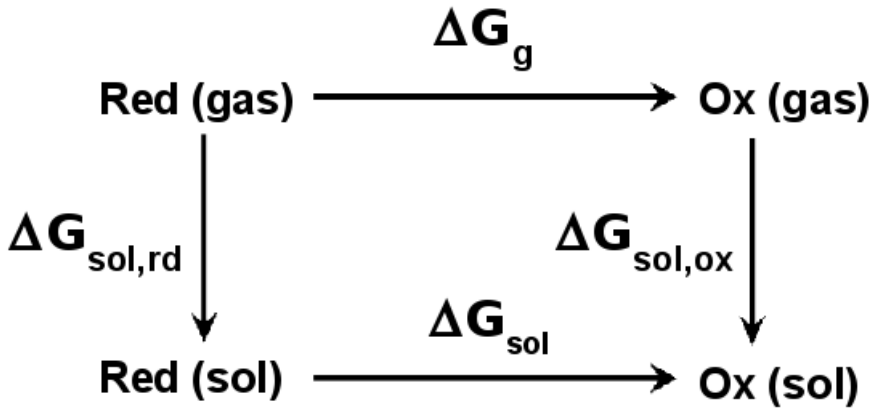

Born-Haber cycle describing the energetics of a redox process using Hess' law.

Figure SI1. DFT optimized structure of $\mathbf{2}^{2-}$ and selected bond distances. Color scheme: Ni: purple; O: red; N: dark blue; C: green and H: white.

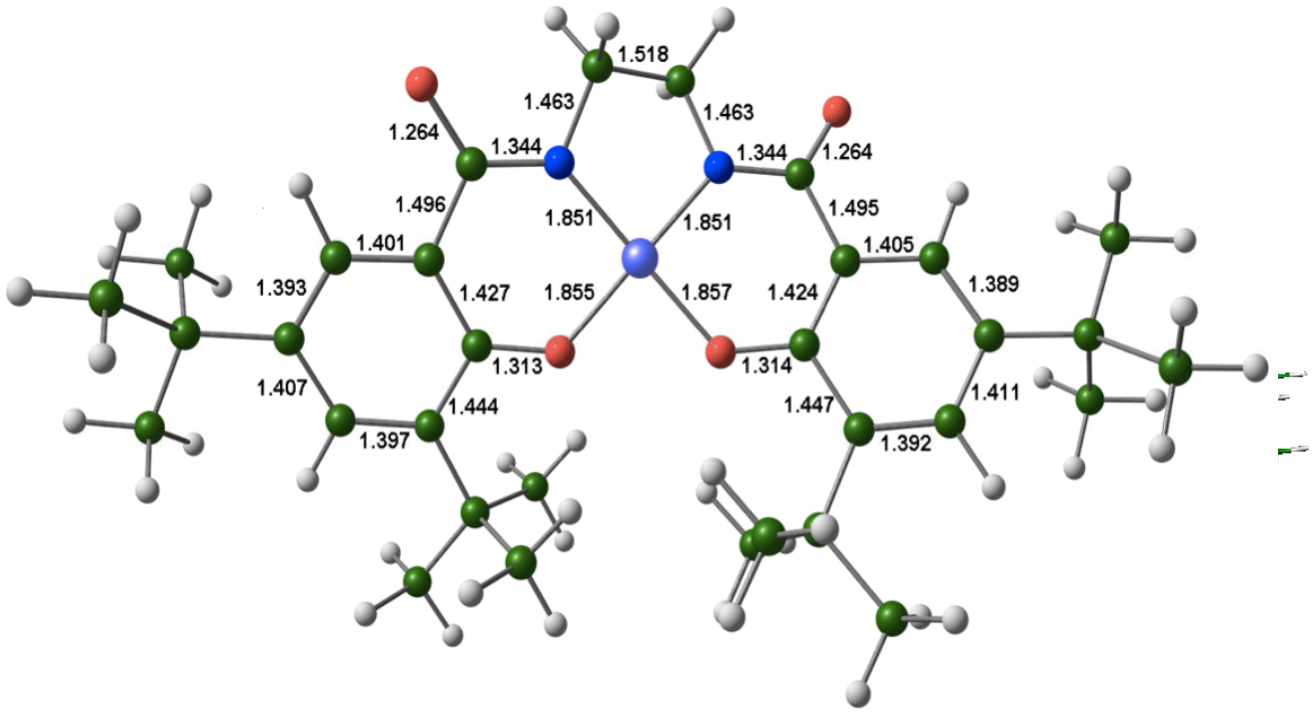

Table SI1. Comparison between experimental and calculated electronic excitations for **1**$^{-}$, **2**$^{2-}$, and **2**$^{-}$.

Complex	Transition	l^{expt}, nm	l^{calcd}, nm	Oscillator strength, *f*	Assignment
$[1]^{-}$	β HOMO-1 → β LUMO	1045	1075	0.053	IVCT
	β HOMO-4 → β LUMO	815	824	0.010	LMCT
$[2]^{2-}$	β HOMO-1 → β LUMO+1	416	463	0.056	MLCT
$[2]^{-}$	β HOMO-1 → β LUMO	1140	1263	0.014	IVCT
	β HOMO-4 → β LUMO	880	908	0.107	LMCT

Figure SI2. Kohn-Sham molecular orbital diagram of $\mathbf{2}^{2-}$ and TD-DFT assignment of the calculated electronic transitions.

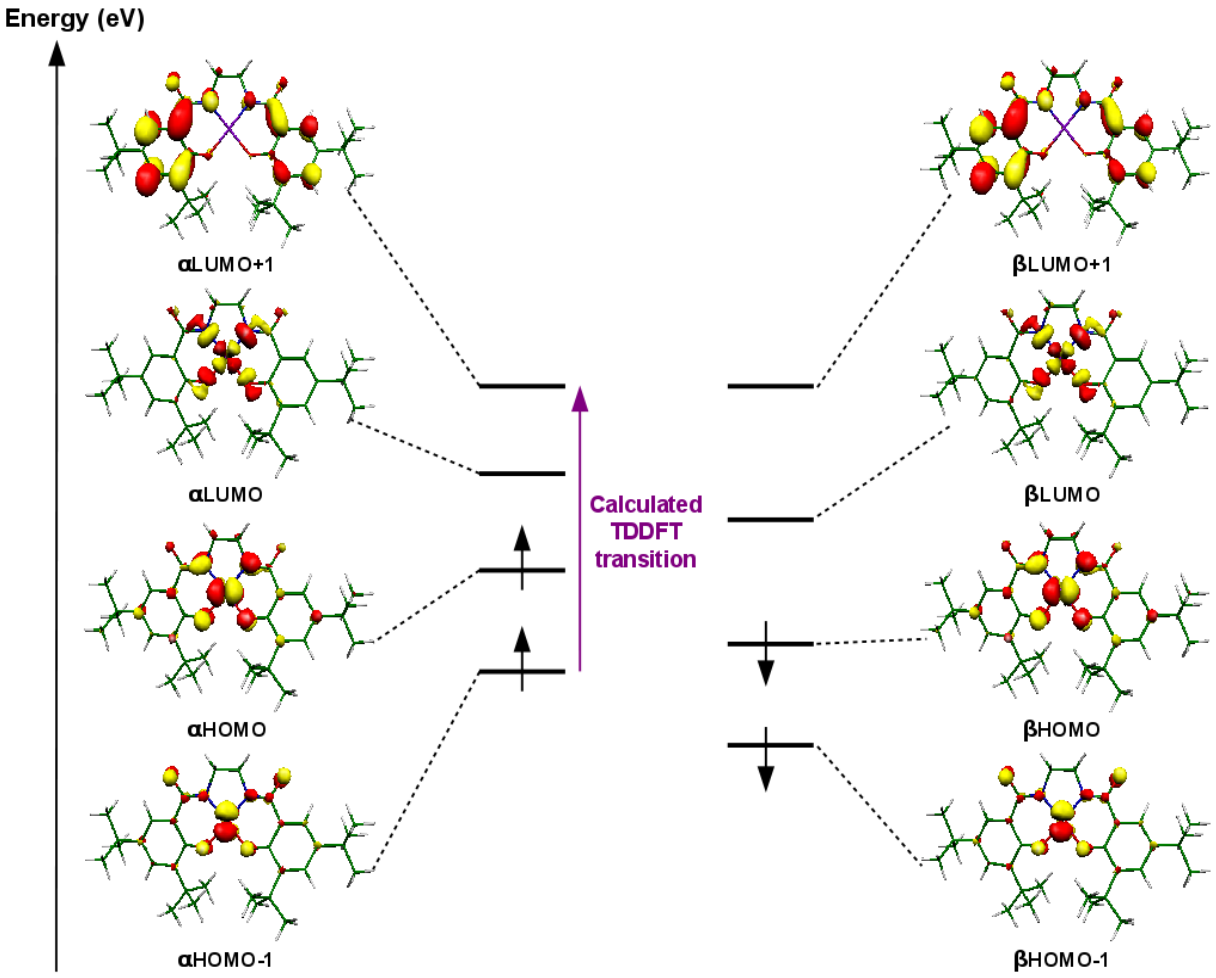

Figure SI3. UV/vis/NIR spectra of electrochemically generated $\mathbf{1}^-$ at 298 K in CH_2Cl_2 (1 mM) (solid line), and $\mathbf{1}^-$ after standing for 15 min at 298 K (dashed lines).

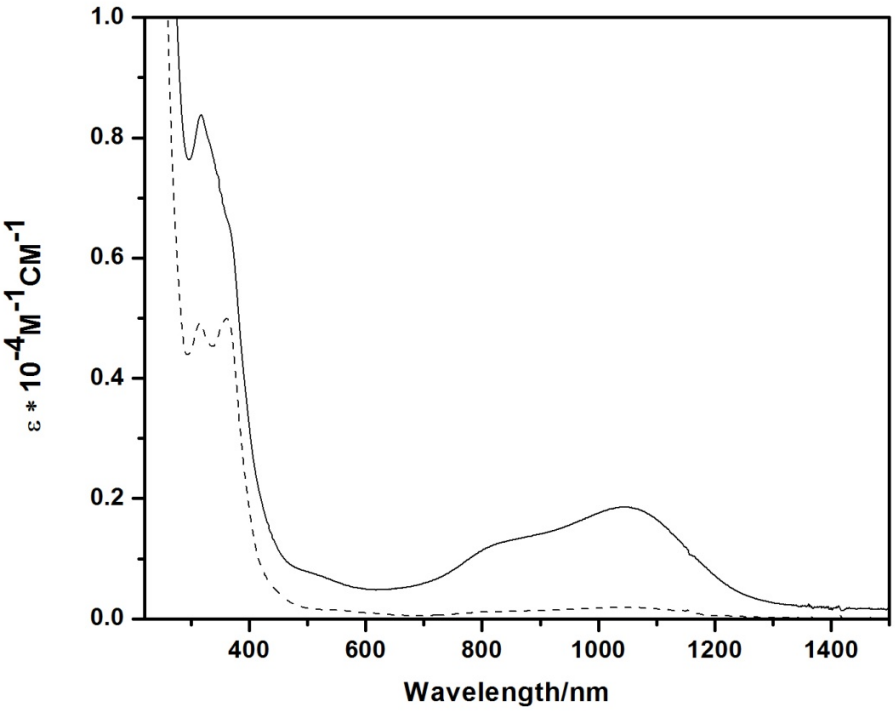

Table SI2. Spectroscopic properties of Nickel complexes in CH_2Cl_2 solution

Compound	λ_{max}/nm(ε/$M^{-1}cm^{-1}$)
$\mathbf{1}^{2-}$	364(7680), 492(sh)(195), 553(sh)(150)
$\mathbf{1}^{-[a]}$	316 (9380), 365(sh)(6520), 815(sh) (1210), 1045(1860)
$[\mathbf{1(Py)_2}]^{-[a]}$	310(sh)(6970), 360(7200), 550(sh) (432), 816(sh)(520), 1044(685)
$\mathbf{2}^{2-}$	319 (6090), 343(sh) (5596), 476 (247), 579(sh) (54)
$\mathbf{2}^{-[a]}$	326(7570), 416(1620), 633(sh)(96), 880(1990), 1140(4450).
$[\mathbf{2}\ (Py)_2]^{-[a]}$	324(sh)(7080), 426(sh)(1370), 880(910), 1358(1760)

[a] UV/vis spectra recorded at RT in the presence of $[NBu_4][PF_6]$ (0.1M).

Figure SI4. DFT optimized structure of $\mathbf{1}^{-}$ and selected bond distances. Color scheme: Ni: purple; O: red; N: dark blue; C: green and H: white.

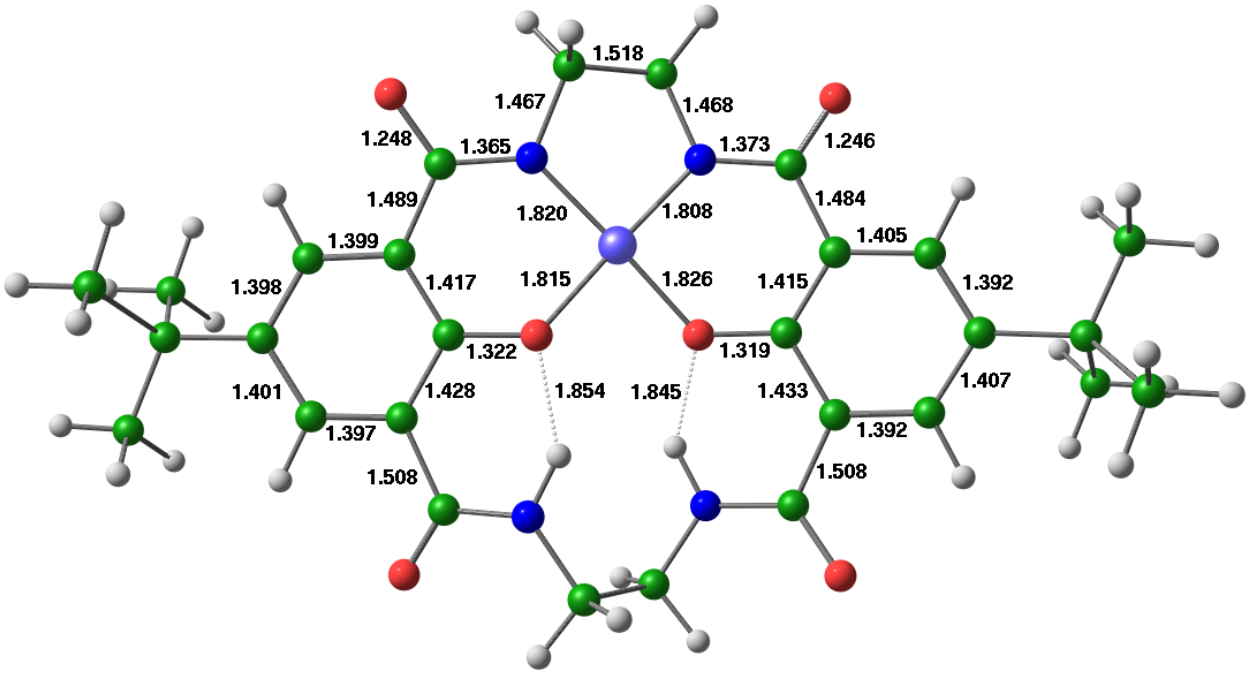

Figure SI5. DFT optimized structure of **2**$^{-}$ and selected bond distances. Color scheme: Ni: purple; O: red; N: dark blue; C: green and H: white.

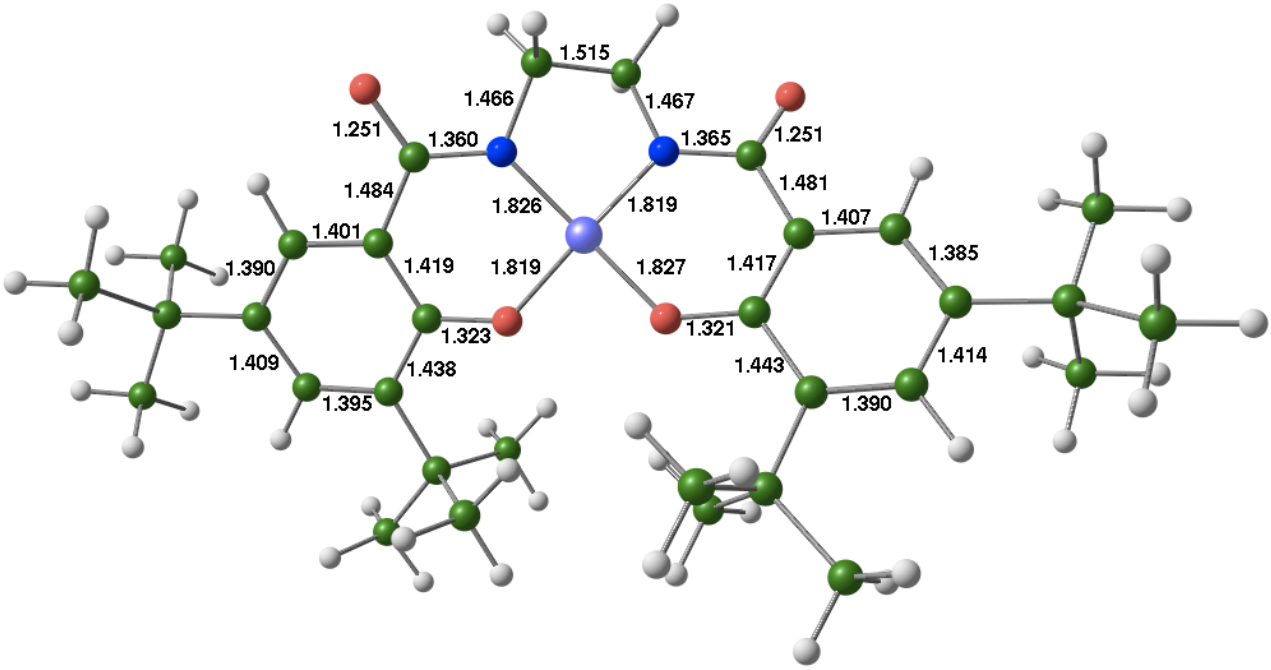

Figure SI6. Kohn-Sham molecular orbital diagram of $\mathbf{1}^{-}$ and TD-DFT assignment of the calculated electronic transitions.

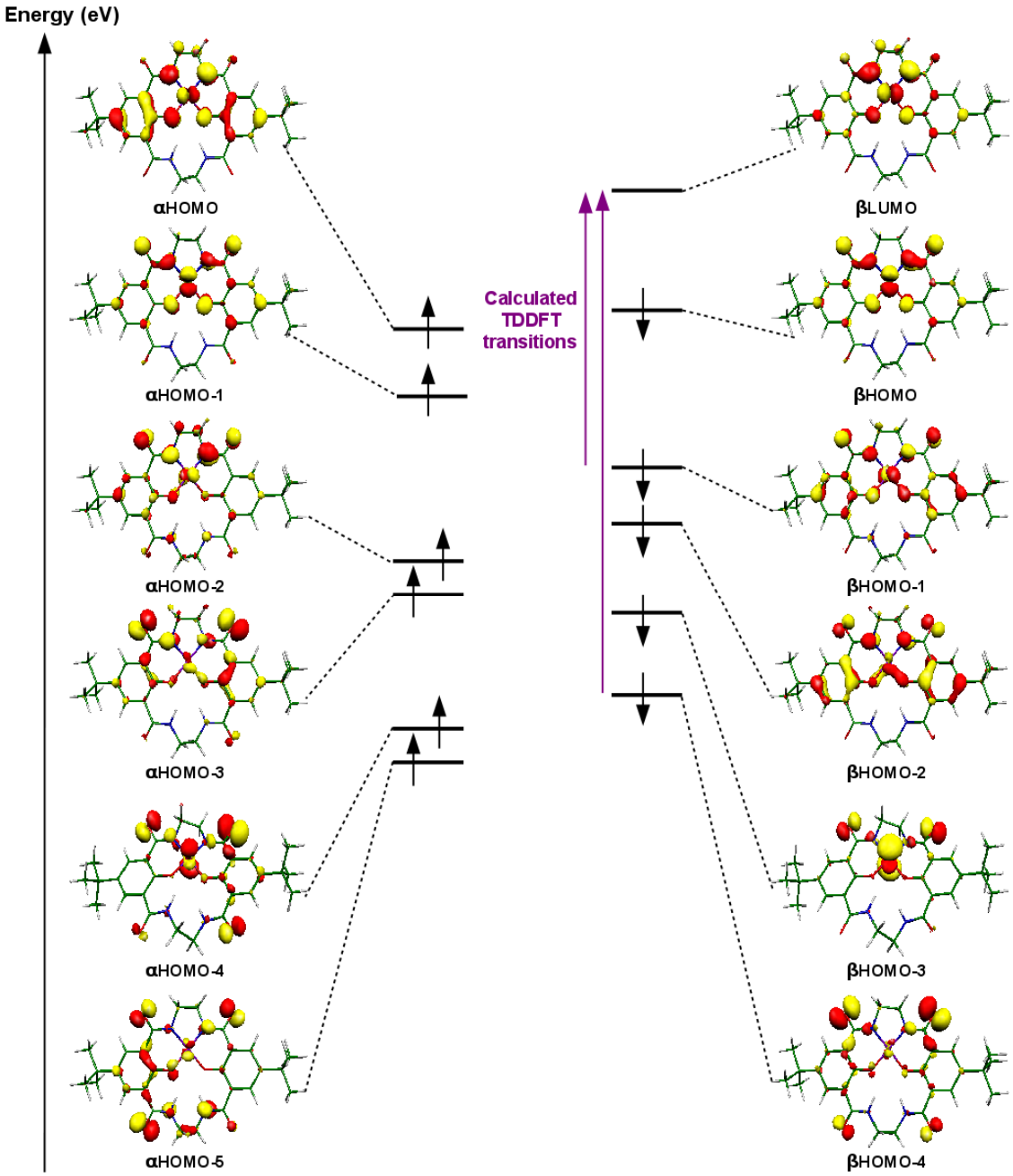

Figure SI7. Kohn-Sham molecular orbital diagram of $\mathbf{2}^{-}$ and TD-DFT assignment of the calculated electronic transitions.

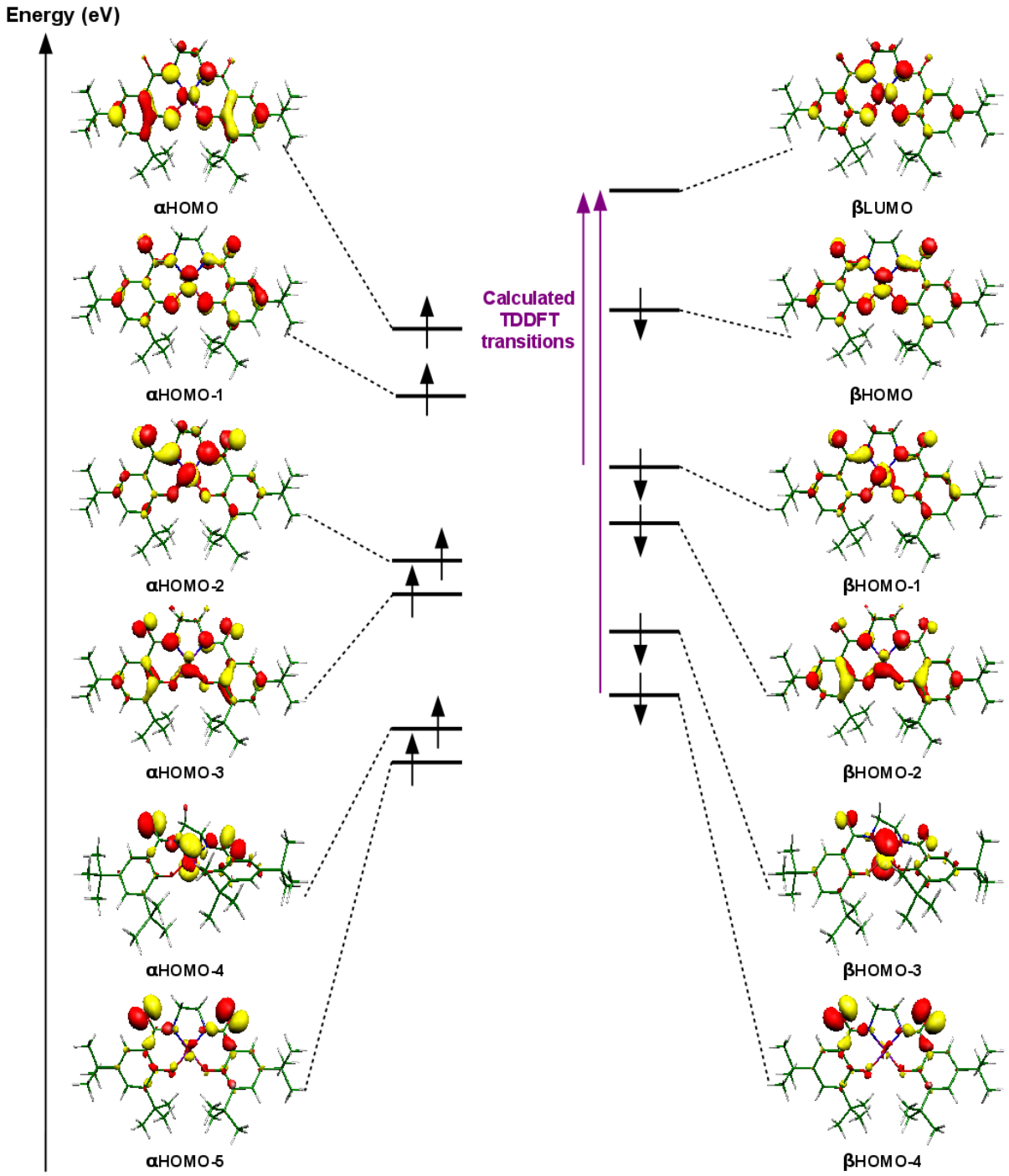

Figure SI8. Spin density plots of $\mathbf{1}^{-}$ (right) and $\mathbf{2}^{-}$ (right).

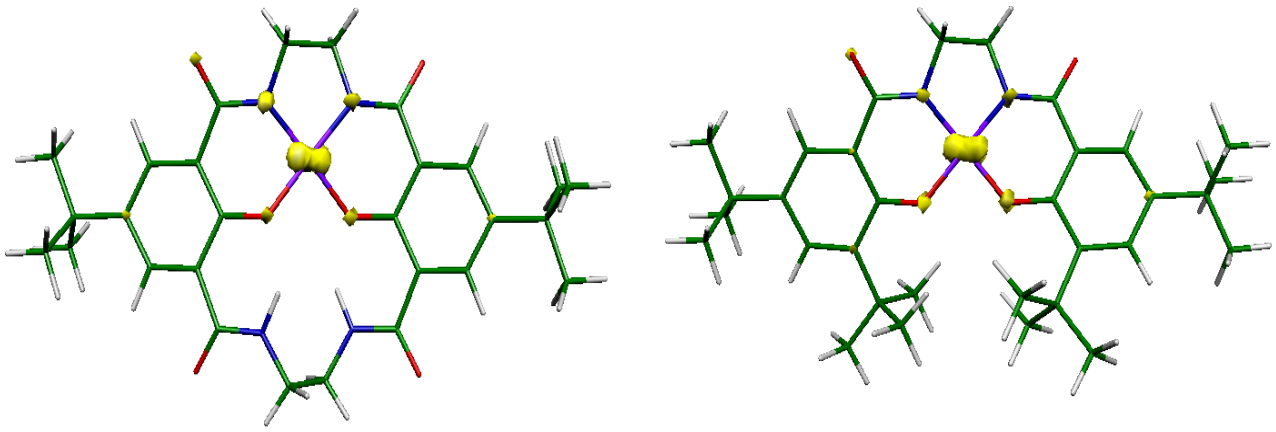

Species	Ni	N1	N2	O3	O4	
$\mathbf{1}^{-}$	0.46	0.12	0.16	0.07	0.05	
$\mathbf{2}^{-}$	0.45	0.09	0.12	0.10	0.08	

Figure SI9. DFT optimized structure of **[1(Py)$_2$]$^-$** and selected bond distances. Color scheme: Ni: purple; O: red; N: dark blue; C: green and H: white.

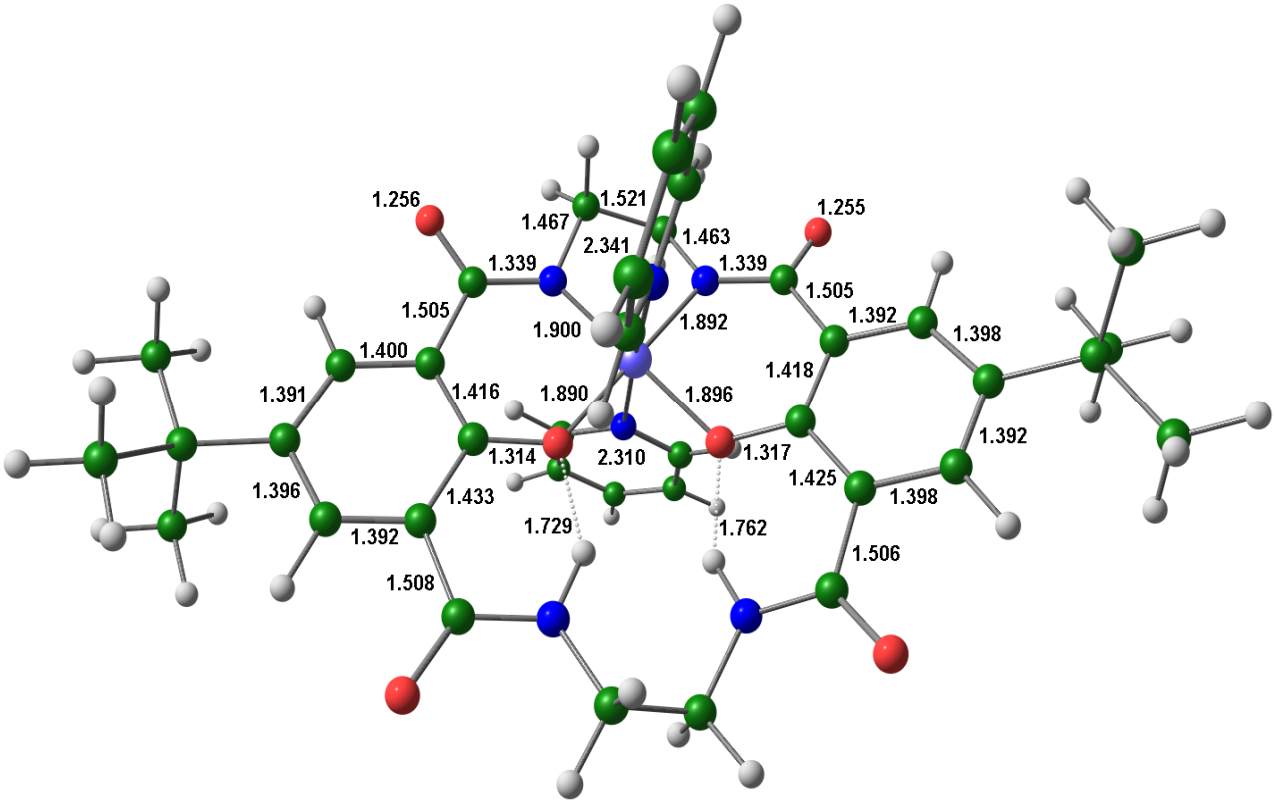

Figure SI10. DFT optimized structure of **[2(Py)$_2$]$^-$** and selected bond distances. Color scheme: Ni: purple; O: red; N: dark blue; C: green and H: white.

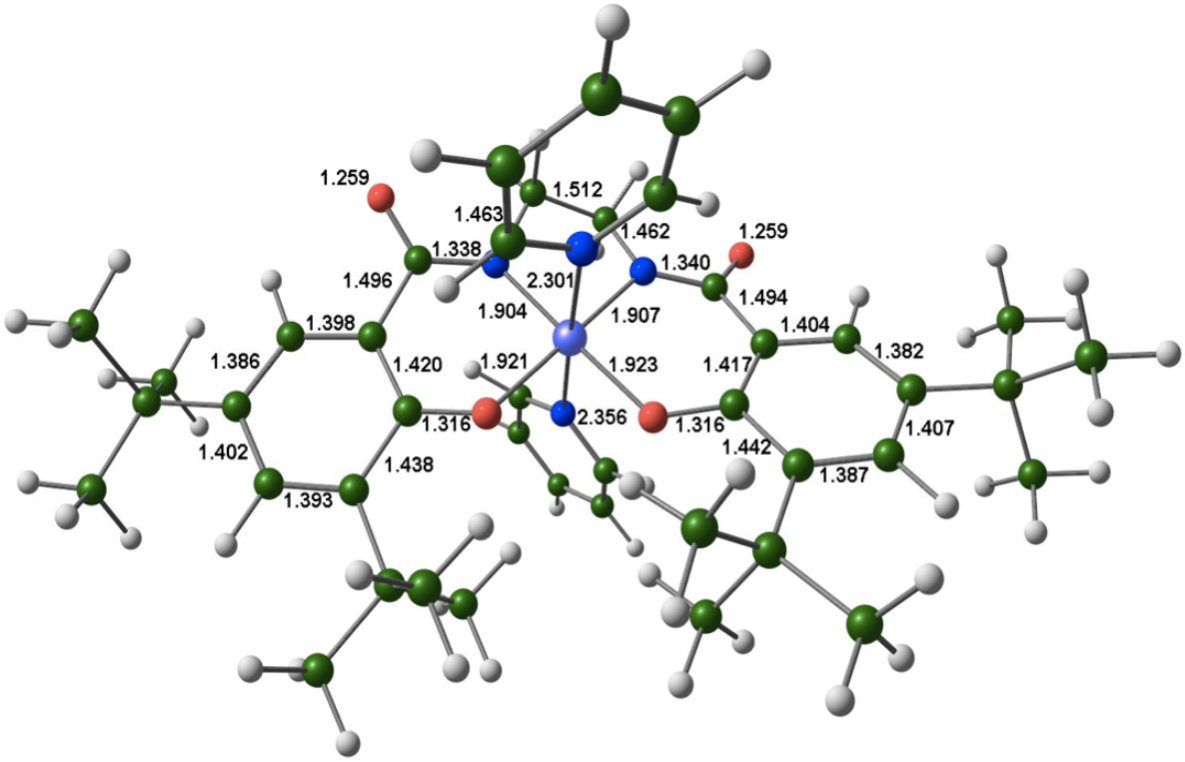

Figure SI11. Spin density plots of **[1(Py)$_2$]$^-$** (right) and **[2(Py)$_2$]$^-$** (right).